

Spectral Features for Re-entry Break-up Event Identification

David Leiser^{*} and Stefan Loehle[†]

High Enthalpy Flow Diagnostics Group, Institute of Space Systems, University of Stuttgart, Germany

Stefanos Fasoulas[‡]

Institute of Space Systems, University of Stuttgart, Germany

The fragmentation of two aerospace aluminum alloys is investigated in a ground testing facility including mechanical loads as occurring due to aerodynamic forces in a real atmospheric entry event at three trajectory points. The emission spectroscopic analysis shows that these materials fail after distinct alkali metal features are observed in the spectra. The two alloys feature characteristic emissions of the different alkali metals. The presence of lithium lines that have previously been exclusively attributed to battery failure in observation campaigns may be considered as a marker for aluminum breakup. This is particularly interesting for future entry observations because it allows a new insight into the structural failure processes of the demising spacecraft. The lack of emission of alloying elements points to these spectra being a candidate for the determination of spacecraft demise. The identification of such features in ground testing will allow a more certain identification of specific break-up events.

I. Introduction

THE missing understanding of the disintegration of spacecraft structures during the atmospheric entry flight is the main driving parameter for the calculation of ground impact risk. Additionally, the full demise of the spacecraft becomes increasingly important, because of the rapidly increasing number of Low Earth Orbit (LEO) which undergo uncontrolled entry after the mission [1]. The recently launched satellite systems such as Starlink and OneWeb with thousands of satellites have furthermore only short lifetimes of 3-5 years which again increases the amount of entering space debris. It is of utmost interest for the space industry to predict the re-entry and demise accurately and space debris problems are a main topic of the European Space Agency under the Space Debris Initiative [1]. One option for the analysis of re-entry processes is the observation of spacecraft during re-entry which gives insight into the processes that dominate fragmentation and ultimately the demise of spacecraft [2]. Another option is to fly on-board systems which analyze the entry in-situ. However, this requires a comparably complex system and the hardware has to be sent to space. Four European Re-entry Break-up Recorders (REBR) were flown, of which three acquired data [3].

^{*}PhD Student, HEFDiG, Institute of Space Systems, Pfaffenwaldring 29, 70569 Stuttgart, Germany, AIAA Member.

[†]Group Leader, HEFDiG, Institute of Space Systems, Pfaffenwaldring 29, 70569 Stuttgart, AIAA Senior Member

[‡]Director, Institute of Space Systems, Pfaffenwaldring 29, 70569 Stuttgart, Germany, AIAA Senior Member.

Finally, the experimental simulation of re-entry demise can be realized in ground testing facilities. In comparison with flight observations, this method allows investigating the particular features of an atmospheric entry leading to the full demise of spacecraft structures. The High Enthalpy Flow Diagnostics Group participated in almost all airborne re-entry observations using different spectroscopic instruments [4–7]. We develop diagnostic methods to be applied in ground testing experiments [8] allowing us to assess the material processes in-situ. With a recently installed load cylinder, the simulation of mechanical forces during the aerothermal testing becomes available. In this study, material samples of the main structural components used in spacecraft were tested under combined aeromechanical and thermochemical loads. During testing the emission spectra of the stagnation point were observed by an Echelle spectrometer in 250 nm–880 nm. The results of the present study show that depending on the mechanical stress and the aerothermal situation, the materials show different features in the spectral data.

II. Experimental Setup

Experiments were conducted in the plasma wind tunnel facility PWK4 at the Institute of Space Systems - IRS [9] at the University of Stuttgart shown in Fig. 1a. The facility consists of a cylindrical vacuum vessel with a diameter of 2 m and a length of 6 m, connected to the central vacuum system with a four stage pump system that allows static pressures in the range of 1 Pa-50 kPa. The plasma is generated by the thermal arc-jet plasma generator RB3, allowing for high local mass specific enthalpy at sufficiently high total pressures. The material samples are 20 mm by 5 mm flat bars with a length of 90 mm mounted between a 5 kN electro-mechanical actuator by *ZwickRoell* and the movable PWK test platform [8].

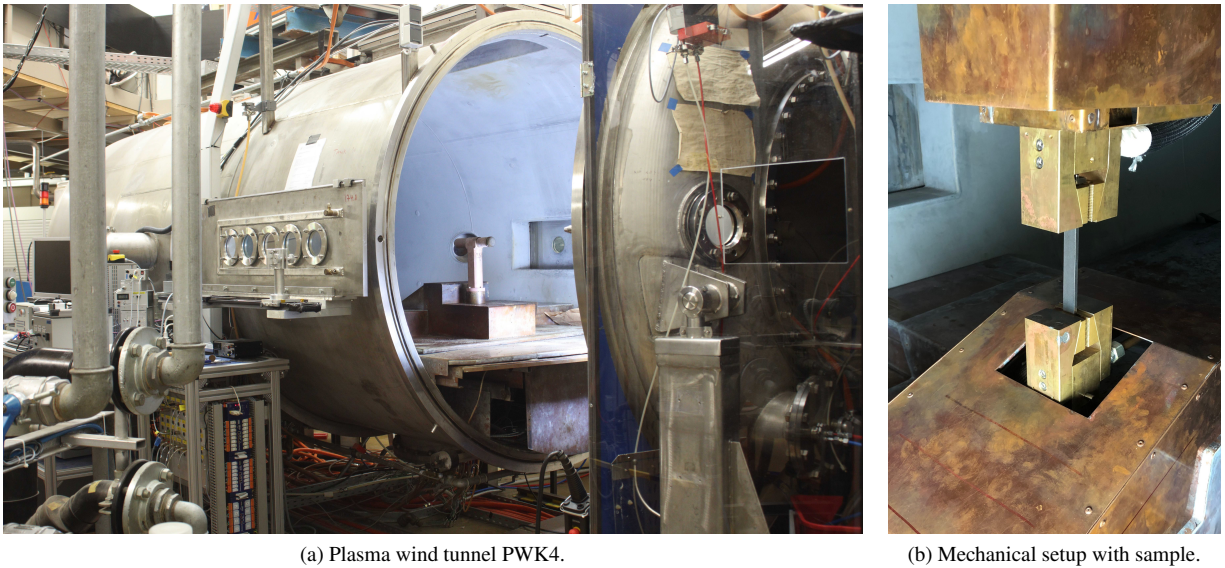


Fig. 1 Test setup at IRS

This setup is shown in Fig. 1b, a flatbar sample is shown in the middle, held by the brass sample holders. The sensitive equipment housed in the plasma wind tunnel is protected from the aggressive environment by water-cooled copper shields with 16 bar high-pressure water, shown above and below the sample holders. The samples are held by serrated grips manufactured out of steel. A pin allows the sample to be loaded with a pre-test clamping force which enables tests under minimal tensile force. The steel grips also functions as a thermal insulator between the samples and the watercooled brass sample holders. This minimizes the contact cooling of the samples.

During the facility startup the probe is positioned outside of the plasma flow. Once the nominal condition is set the probe is moved to the center of the flow.

Two main types of tests were conducted, denoted as scenario 1 and 2. During scenario 1 tests, the samples are held in the plasma at minimal force < 10 N until the sample fails due to melting or it reaches an isothermal state. Scenario 2 tests are conducted by applying the nominally expected force as determined from the re-entry trajectory [10]. If the sample reaches an isothermal state in either scenario, the load is increased linearly until the sample fails.

A. PWK Flow Condition

The flow conditions correspond to the re-entry trajectory of Sentinel-2 [11], which falls into the ESA standard trajectory corridor [12, 13], at an altitude of 65, 75 and 90 km. Figure 2 shows the simulation and the chosen points for ground test simulation. These conditions were chosen as representative of three characteristic trajectory points on a re-entry from Low Earth Orbit [14, 15]. The 90 km point is early during re-entry and features small heat loads and the

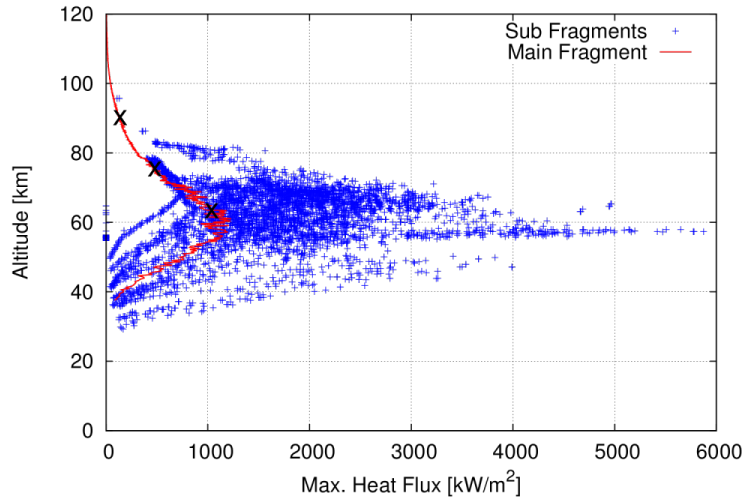


Fig. 2 Re-entry fragmentation simulation of Sentinel-2 (courtesy HTG).

separation of outlying elements such as solar panels. 75 km is around the break-up altitude with major fragmentation of the main structure of spacecraft. Peak heating occurs around 65 km, this is a major factor in further structural break-up leading to subsystem release and determining the demise of components.

Table 1 Generator and flow condition corresponding with the trajectory points.

Condition		90 km	75 km	65 km
Generator conditions		Unit		
Arc current	A	350 ± 5	545 ± 4	500 ± 2
Arc voltage	V	85 ± 2	90 ± 4	98 ± 2
Mass flow rate	g s^{-1}	4.00 ± 0.01	5.00 ± 0.01	6.52 ± 0.01
Ambient pressure	Pa	35 ± 1	201 ± 1	1250 ± 5
Test conditions		Unit		
Reference distance	mm	310.0 ± 0.1	310.0 ± 0.1	185.0 ± 0.1
Heat flux	kW m^{-2}	120 ± 2	497 ± 5	843 ± 5
Stagnation pressure	Pa	177 ± 2	1352 ± 4	4690 ± 10

The conditions necessary to obtain these trajectory points were determined by matching the heat flux and total pressure from flight to ground. The tunnel conditions are characterized using a flat faced 50 mm diameter axisymmetric total pressure and heat flux probe [16] machined from copper. The measured conditions are scaled to the aluminum flat bar samples using local heat transfer simulation scaling [17] and correcting for the difference in catalycity [18]:

$$\dot{q}_{\text{flatbar}} = \dot{q}_{\text{axisymmetric}} \sqrt{\frac{2.5}{4}} \quad (1)$$

The detailed approach for the translation of the flight situation to the flat bar testing in the ground testing facility are described in a different paper [19]. Thereby the condition on the flat bar equals the flight condition. The reference conditions, generator settings and resulting conditions are displayed in table 1.

B. Investigated Materials

Aluminum is the main element of most satellite structures, used for all manner of lightweight structures. Two well characterized alloys that are used extensively are Al-6060 and Al-7075 [20]. The alloying elements according to DIN EN 573-3 [21] are shown in table 2

Table 2 Aluminum alloys and their main alloying elements in mass percent.

	Al	Si	Fe	Cu	Mn	Mg	Cr	Zn	Ti	other
Al-6060	remainder	0.3–0.6	0.1–0.3	0.1	0.1	0.35–0.6	0.05	0.15	0.10	0.15
Al-7075	remainder	0.4	0.5	1.2–2.0	0.3	2.1–2.9	0.18–0.28	5.1–6.1	0.2	0.15

C. Diagnostic Setup

Figure 3 shows the schematic of the experimental setup in PWK4 at IRS. The mechanical cylinder [8] holds the sample at the reference distance from the generator nozzle (see table 1).

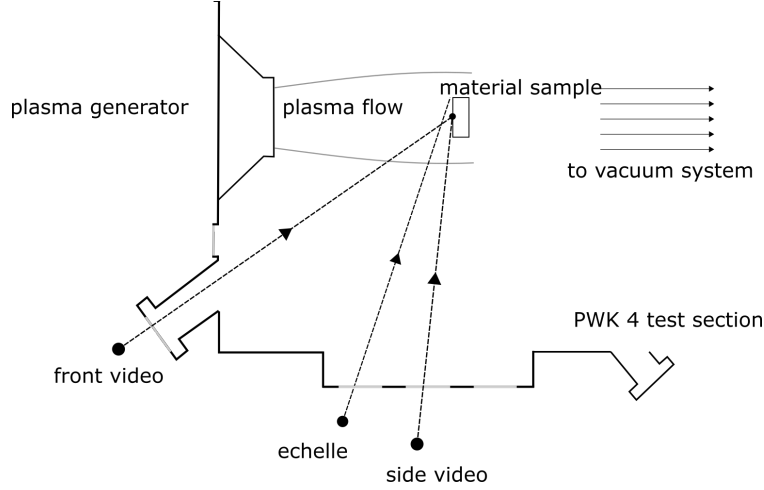


Fig. 3 Schematic diagnostic setup of PWK4 (top view).

The front and side windows are used for *Canon EOS 5DSR* digital cameras for a direct visual investigation. Sample

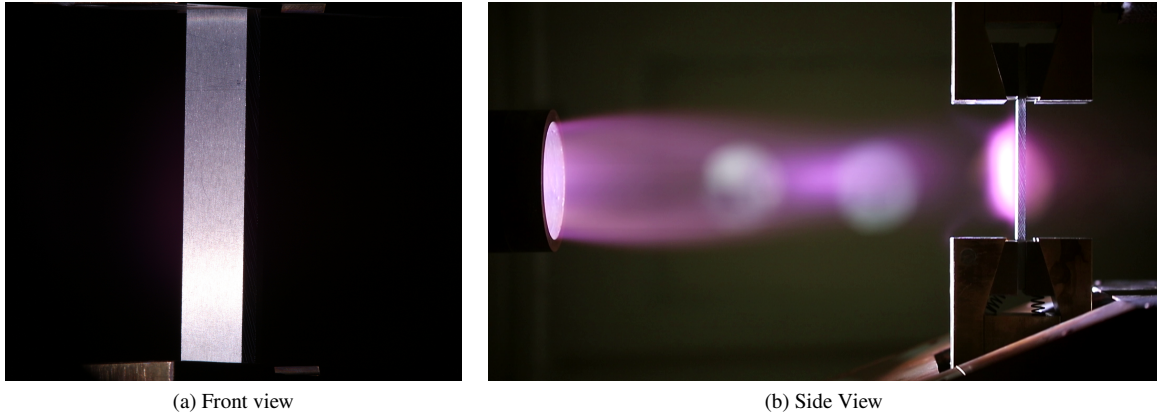


Fig. 4 Still frame of the video imaging system

images recorded by the video imaging system are shown in Fig. 4. The front view (Fig. 4a) allows an in-depth analysis of the sample while the side view (Fig. 4b) allows better insight into the plasma flow specifically discoloration.

An *LTB Aryelle 150* Echelle spectrometer [22] is used to record the spectra in the range of 250 nm–880 nm. The setup of the optical system is shown in Fig. 5.

A 50 mm lens tube with an achromatic lens optimized between 450 nm–900 nm captures the emission radiation and focuses it onto a 50 μ m fiber optic cable port. This leads to the slitless spectrometer entry port. No further apertures or filters were used for this campaign.

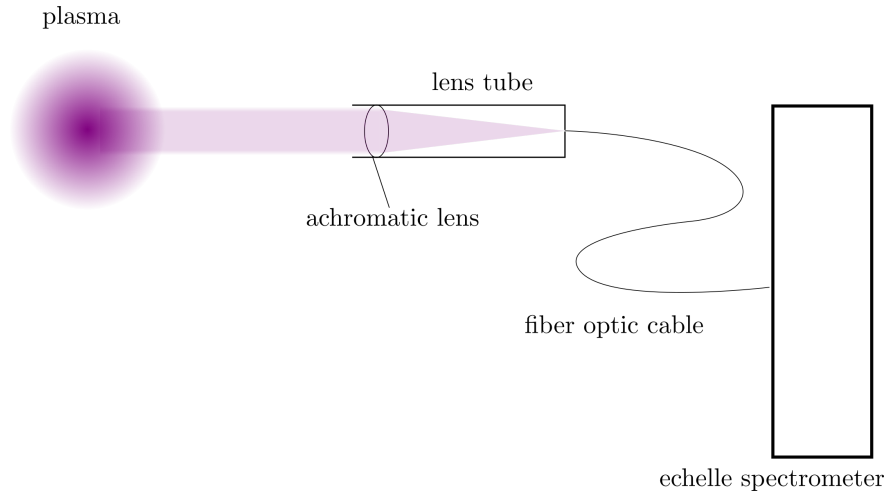


Fig. 5 Overview of the optical setup of the Echelle spectrometer system.

The spectrometer optics are aligned to record the emissions from the stagnation point ahead of the surface of the material sample. This alignment prevents the spectrometer from recording the Planck radiation of the hot sample while capturing all of the immediate stagnation point emission in the gas phase.

The advantage of an Echelle spectrometer is its high spectral resolution over a long wavelength interval. This is realized by taking spectra at very high orders (40-60) which subsequently are aligned vertically on the detector chip. The system used here was designed to detect UV-NIR without any gaps. Since it is used in airborne observations, a compact system is required. The camera connected to the spectrometer is an EMCCD (Qimaging Rolera) with a minimum exposure time of 1 ms. Within one order the sensitivity has a central peak, so that aligning the spectra results in the spectra as shown in Fig. 6.

The wavelength of the spectrometer was calibrated with a mercury-argon lamp. The intensity calibration of the system is realized by positioning an Ulbricht sphere (Gigahertz Optics BN0102) at the location of interest in the tunnel. A spectrum is recorded (Fig. 6b) and time normalized. The known radiance of the calibration lamp (Fig. 6a) results in a wavelength dependent calibration factor. This calibration factor can be applied to a time normalized spectrum (Fig. 6c), resulting in a calibrated spectrum (Fig. 6d). The sensitivity peaks within one spectral order can not be removed completely without losing spectral information at the same time. Therefore the resulting spectra always contain a small fraction of this intensity distribution over the observed order.

The manner in which the diffraction orders are projected onto the camera chip can also lead to order cross-talk, meaning that the software attributes the signal to the wrong diffraction order and therefore the wrong wavelength. Such an error occurred during parts of this campaign. The effect appeared at wavelengths upwards of 550 nm. While this makes the absolute intensity calibration impossible, the relative temporal evolution of lines is not affected by this error.

A sample spectrum of a stagnation point plasma on a cool wall is shown in Fig. 7 in the wavelength range of

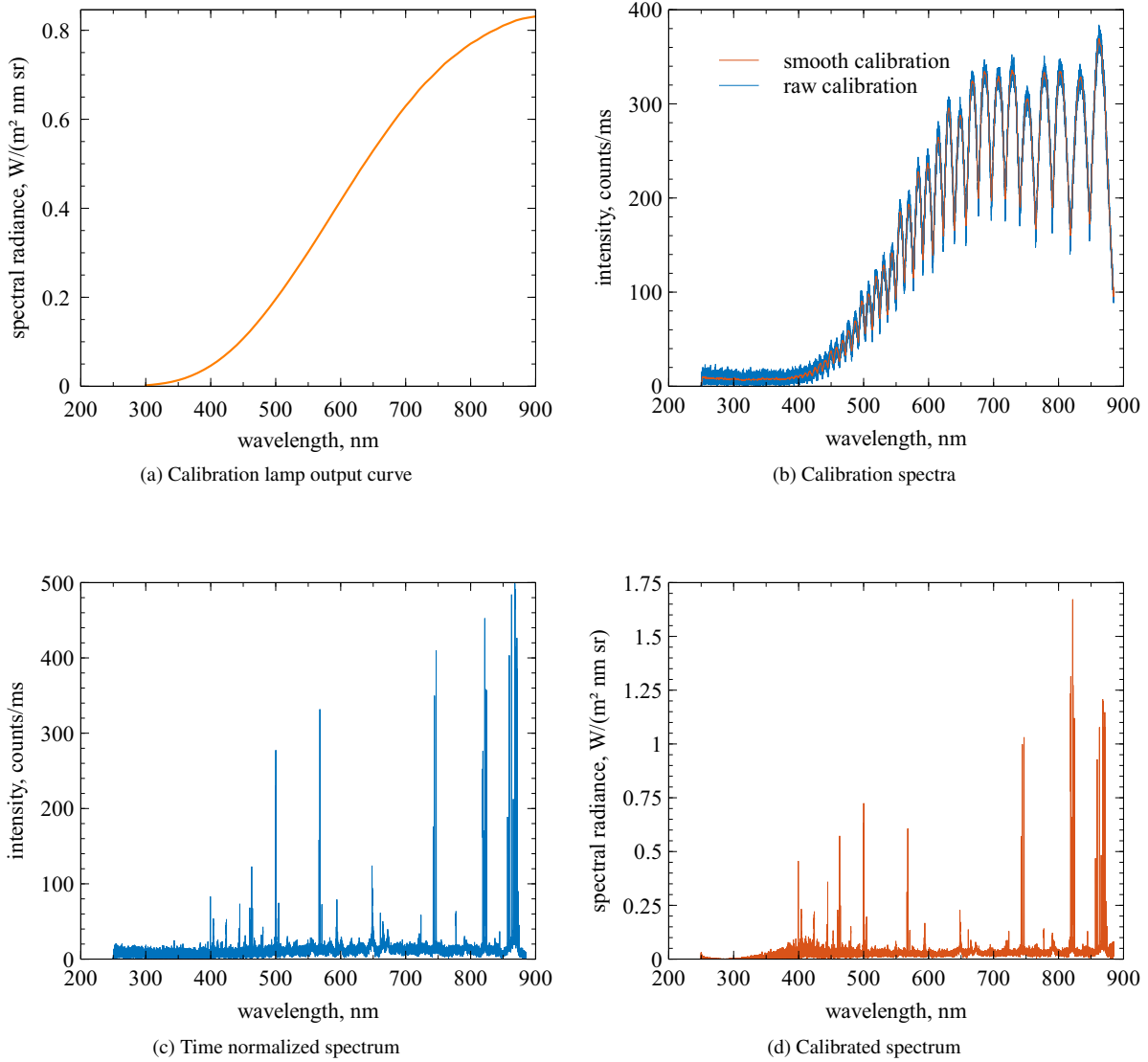


Fig. 6 Echelle calibration overview

730 nm–810 nm to show the prominent atomic lines that correspond to oxygen triplet at 777 nm and the nitrogen lines 742 nm–747 nm.

The misinterpreted lines are visible at 804 nm, which can be attributed to the 777 nm oxygen triplet as well as erroneous lines between 765 nm–775 nm, which correspond to the nitrogen lines between 742 nm–747 nm. Spectra that show this double appearance of lines are annotated in section III.

After the error was identified, the spectrometer system was readjusted. This led to a better signal, which allowed the system to be operated with a lower gain than during the initial part of the campaign. The lower gain led to less pronounced noise in the data and a better signal to noise ratio at comparable exposure times in the latter half of the

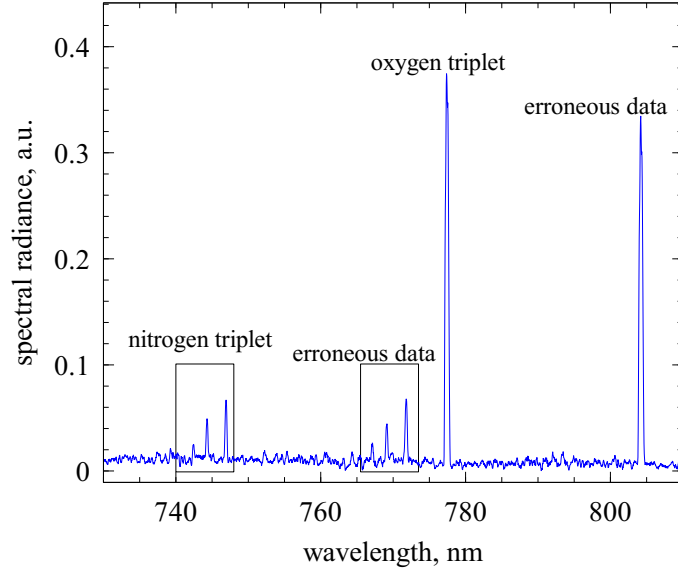


Fig. 7 Sample spectrum.

campaign.

III. Spectral Data Analysis

The temporal development of the line intensity was determined by integrating the spectral lines over its total width. For this, the central line position was determined around the expected spectral position (see table 3) taken from the NIST database [23].

Table 3 Center wavelength of the evaluated spectral lines for each species [23].

element	symbol	wavelength, nm	transition
oxygen	O	777.42	(triplet) $3p - 3s$
nitrogen	N	746.90	$3p - 3s$
aluminum	Al	396.15	$4s - 3p$
magnesium	Mg	518.36	$4s - 3p$
silicon	Si	728.92	$3p(^2P_{3/2})4f - 3p^3$
zinc	Zn	481.05	$5s - 4p$
copper	Cu	521.82	$4d - 4p$
iron	Fe	438.35	$4p - 4s$
lithium	Li	670.78	(doublet) $2p - 2s$
sodium	Na	589.00	$3p - 3s$
potassium	K	766.49	$4p - 4s$

The line width was determined by fitting a Voigt function for the detected lines. The Voigt function is approximated using the methods of Liu et. al [24] as well as Olivero and Longbothum [25]. Using a non-linear regression algorithm the Gaussian and Lorentzian widths are determined for each spectrum. The result of a line determination and fit is shown exemplary at a sodium line in Fig. 8. The integration limits were chosen to avoid other lines close to the observed one.

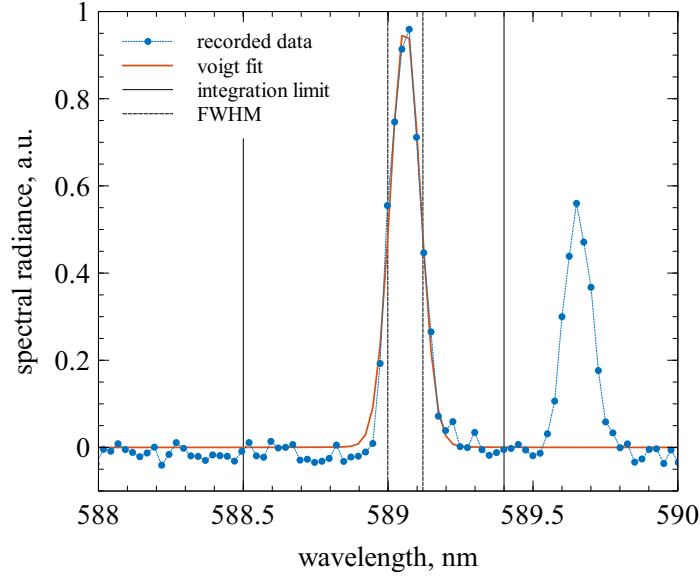


Fig. 8 Recorded data with a Voigt fit of a sodium line, FWHM and integration limits.

Molecular bands were identified using the database by Pearse and Gaydon [26], these were not evaluated further.

The onset of the experiment and test time $t = 0$ s is determined by the probe reaching the center of the flow. The atomic lines and bands that are visible in all experiments correspond to N, N^+ , N_2 , N_2^+ , O, and O_2 , as expected from the air plasma. The variations of intensity over time are weak and common for such experiments [27].

A. Aluminum 6060

1. 65km

Figure 9 shows a still frame of the aluminum 6060 test at 65 km with force scenario 1 shortly before the material failure. The front view (Fig. 9a) shows the bulk material melting with the thin oxide layer holding the sample together, the deformation of the sample surface is visible here. An image shortly later is shown in the side view (Fig. 9b), with molten material being ejected into the wake. While a strong discoloration is especially visible in the wake, it is also visible in the stagnation region.

Spectral data collected during the 65 km experiments is shown in Fig. 10. Figure 10a shows five sample spectra recorded throughout the experiment conducted with negligible force (scenario 1). For better visibility, the spectra are

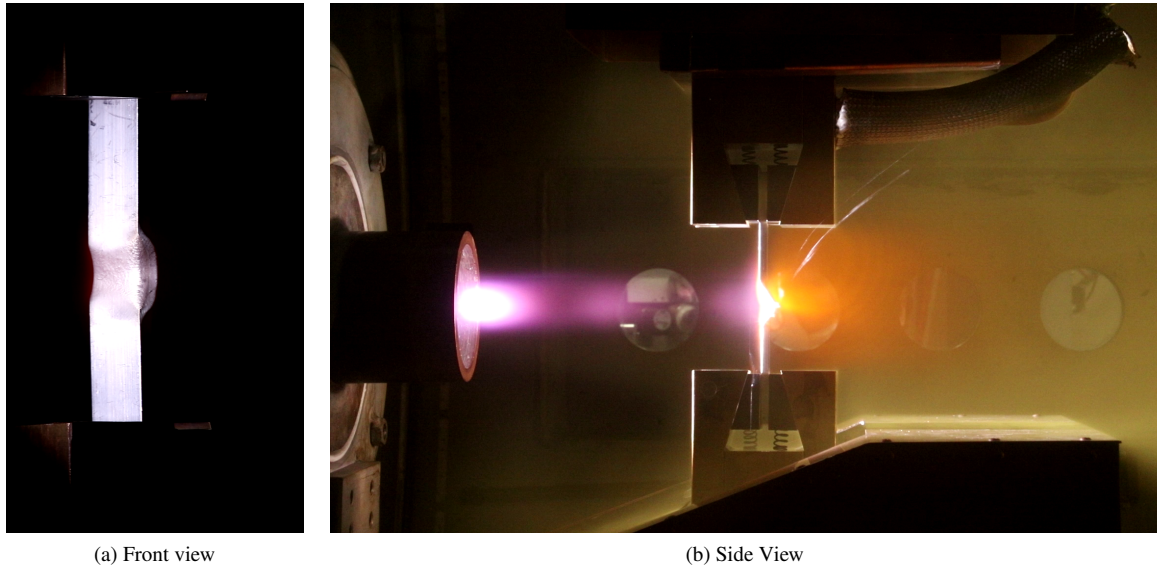


Fig. 9 Still frame of aluminum 6060 test at 65 km Scenario 1

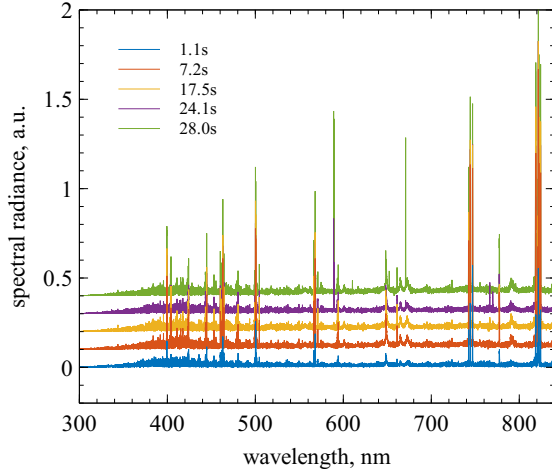
offset to one another. The temporal evolution of the integrated line intensity is shown in Fig. 10b with the air plasma lines shown on top and the alloy constituents on the bottom. Spectra recorded during the experiment with nominal forces (scenario 2) applied is displayed in Fig. 10c, the respective time evolution is shown in Fig. 10d.

During both tests, no spectral signatures of the alloy were visible. A weak emission line corresponding to K appears, after around 15 s in both experiments. Shortly afterwards the prominent Na line appears and gradually gets stronger. In scenario 2 the probe fails due to the applied forces, at around 23 s while in scenario 1 the Na line intensity increases until it saturates the spectrometer at 26 s. In the scenario 1 test, at around 24 s, the bulk material melted, determined by the video data which corresponds to the Li line appearing. This line grows in intensity, until the material failed at the end of experiment, $t = 28$ s. In scenario 2, Li is visible for a few frames very weakly shortly before the sample fails.

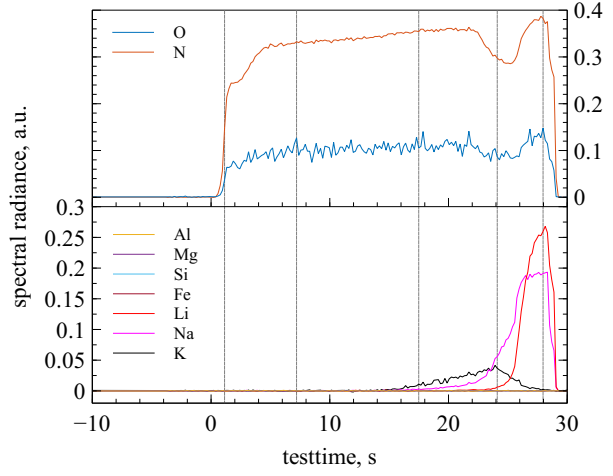
2. 75km

Data collected during the experiments at 75 km is shown in Fig. 11. These experiments were conducted during the first part of the campaign.

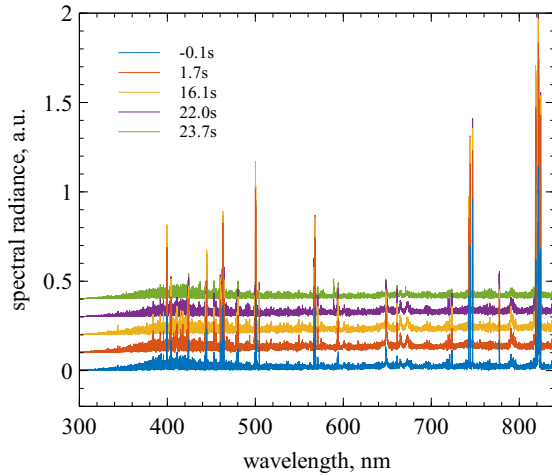
Similar effects as during the 65 km condition can be seen here, no alloy components are spectrally active, for the beginning of the test it is purely the plasma constituents. During the test a weak K signature was detected, starting at 15 s during the scenario 1 test and at 10 s during the scenario 2 test. In both tests the intensity peaks within 3 s and diminishes over a further 4 s. Na is also discernible in both experiments with the onset fairly similar at 16 s and 13 s respectively. During the scenario 1 test the intensity reaches a plateau between 20 s–21 s and diminishes together with material deformation and failure. During scenario 2, the intensity of Na increases towards the failure time, though the slope of the line seems to indicate that the peak intensity and a potential plateau lies around the failure time. In both



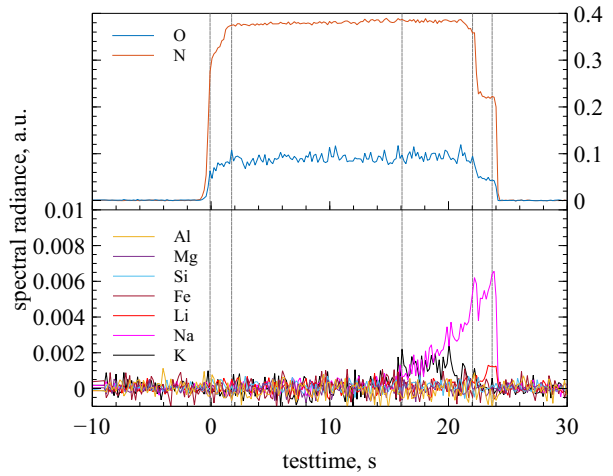
(a) Scenario 1 spectra at five test times of interest, marked in Fig. 10b



(b) Scenario 1 spectral radiance of the individual lines over time



(c) Scenario 2 spectra at five test times of interest, marked in Fig. 10d



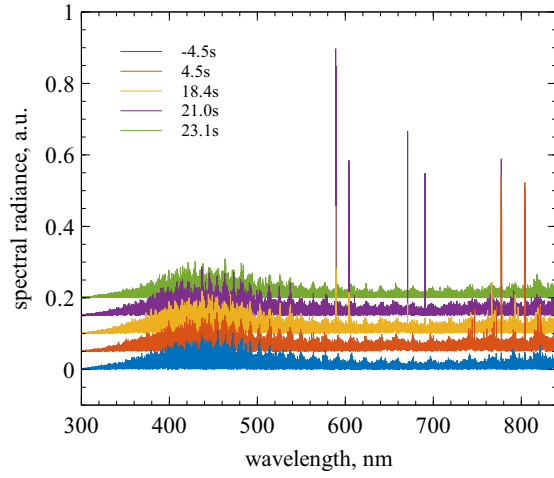
(d) Scenario 2 spectral radiance of the individual lines over time

Fig. 10 Echelle data of Al-6060 at 65km

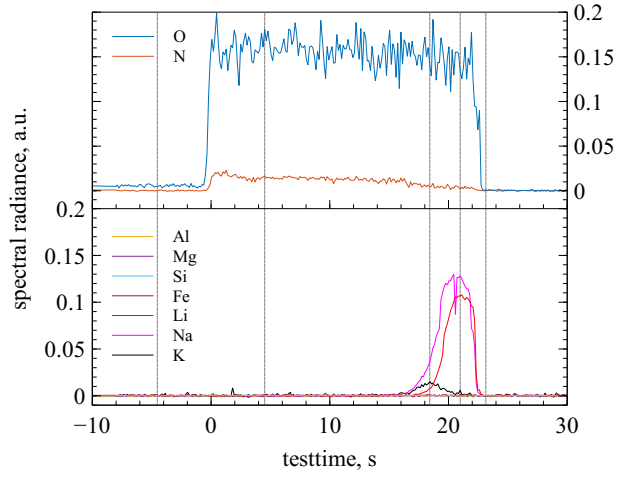
tests, Li appears at around 18 s, with the intensity increasing rapidly. During scenario 1 the intensity peaks around 21 s and diminishes with the material deformation and failure, while during scenario 2 the probe fails with the intensity reaching a peak.

3. 90km

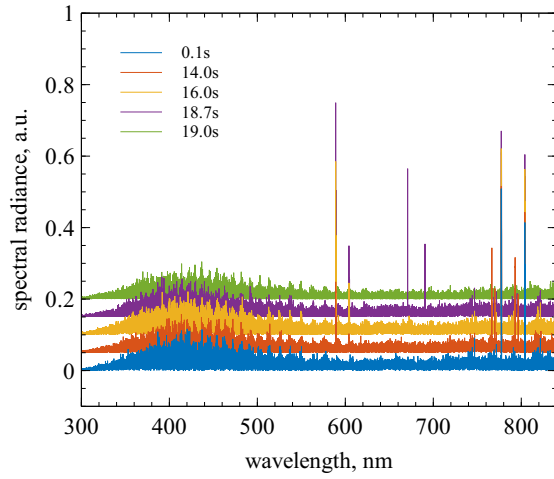
Data collected during the 90 km condition experiment is shown in Fig. 12. Since the material sample did not fail at the nominal force (load scenario 1), the force was further increased until the material failed. The data collected during this test is very noisy, due to the high gain settings chosen for the very weak emission. More importantly, the condition



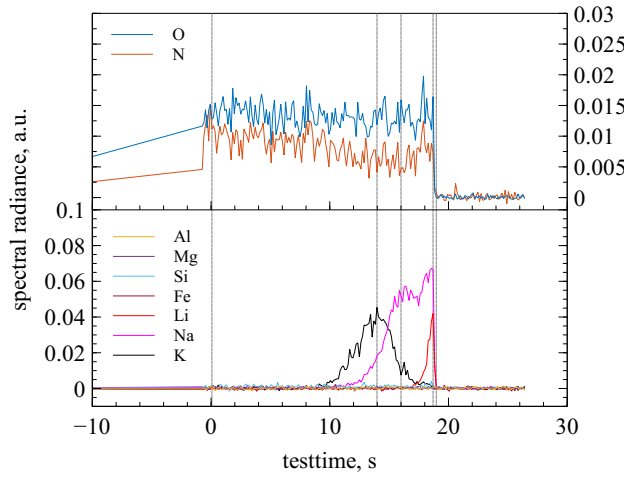
(a) Scenario 1 spectra at five test times of interest, marked in Fig. 11b



(b) Scenario 1 spectral radiance of the individual lines over time



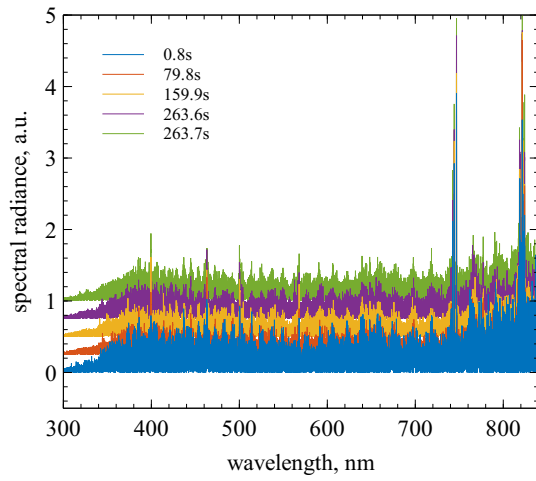
(c) Scenario 2 spectra at five test times of interest, marked in Fig. 11d



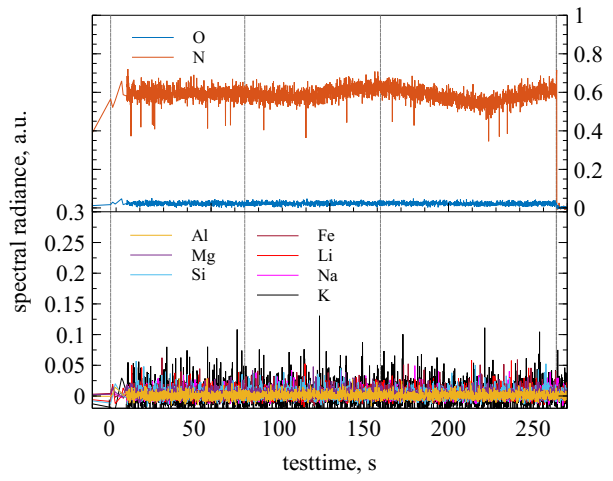
(d) Scenario 2 spectral radiance of the individual lines over time

Fig. 11 Echelle data of Al-6060 at 75km

exhibits a low total pressure and low heat flux, which results in very weak plasma lines. Aside from these, no lines were distinguishable during testing.



(a) Spectra at five test times of interest, marked in Fig. 12b



(b) Spectral radiance of the individual lines over time

Fig. 12 Echelle data of Al-6060 at 90km Sz1/2

B. Aluminum 7075

1. 65km

Data collected during the 65 km experiments is shown in Fig. 13.

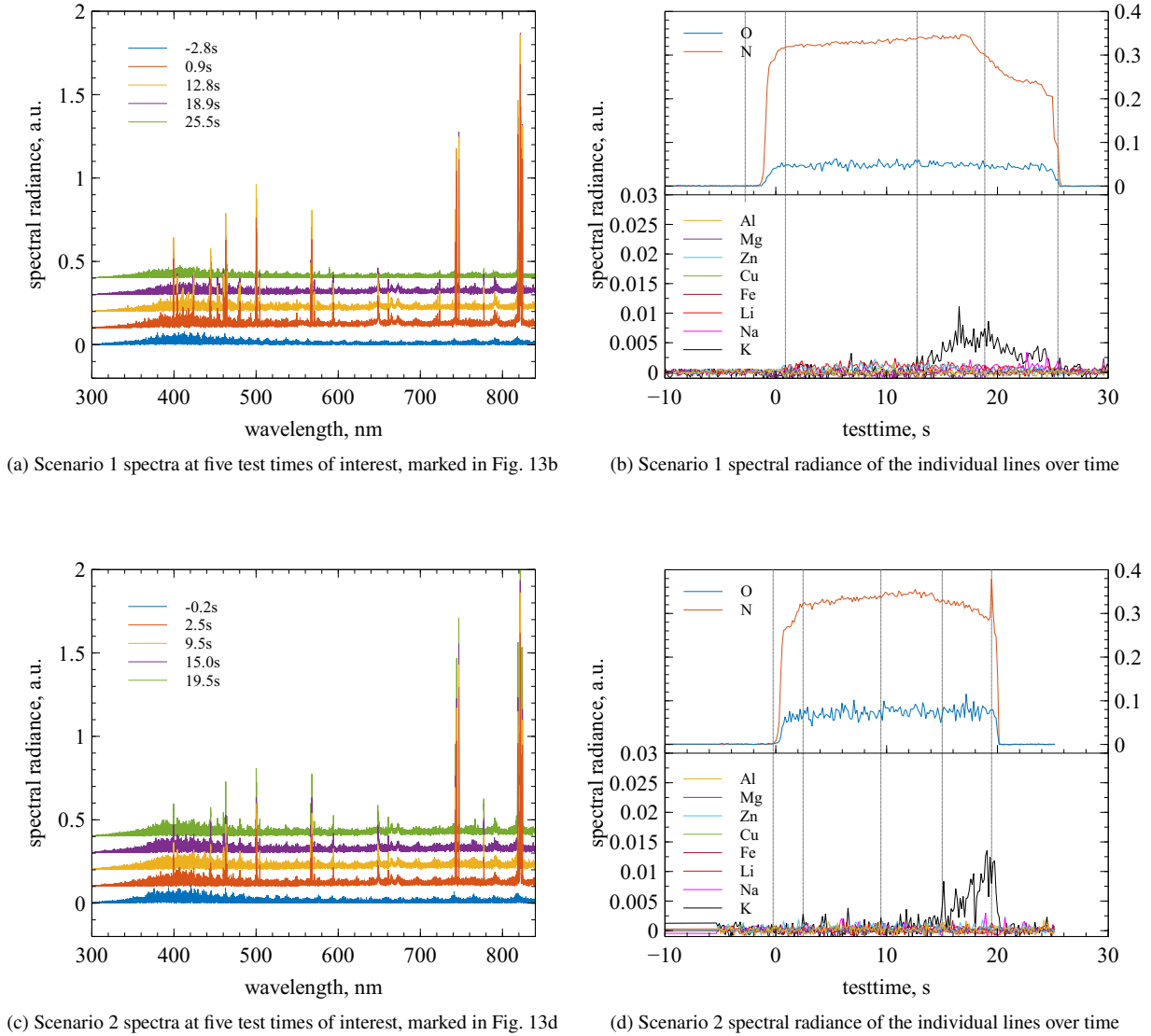


Fig. 13 Echelle data of Al-7075 at 65km

During both tests, the most prominent lines and bands correspond to the air plasma species, most prominently N and N^+ . This is the same observation made during the Al-6060. At about 14 s a weak K signature appears. During the scenario 1 test, the K line intensity peaks at 19 s and decreases toward the end of the experiment at 25 s. In the scenario 2 test the experiment ends after 20 s, at this point the K line intensity has peaked. The evolution of the lines is almost identical up to the point of failure. No further elements were discernable in the spectral analysis.

2. 75km

Figure 14 shows a still frame of the aluminum 7075 test at 75 km with force scenario 1 shortly before the material failure. The front view (Fig. 14a) shows the sample failing, it is unclear if the material is molten since the probe is deformed significantly while the surface shows cracks. An image at the same time is shown in the side view (Fig. 14b). A strong discoloration is visible in both the stagnation region and the wake.

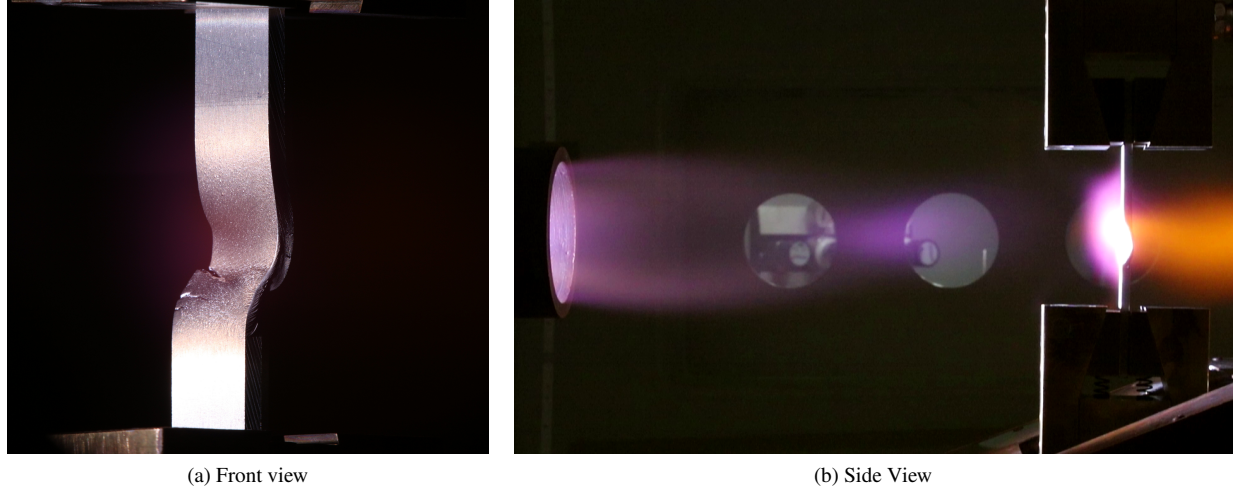


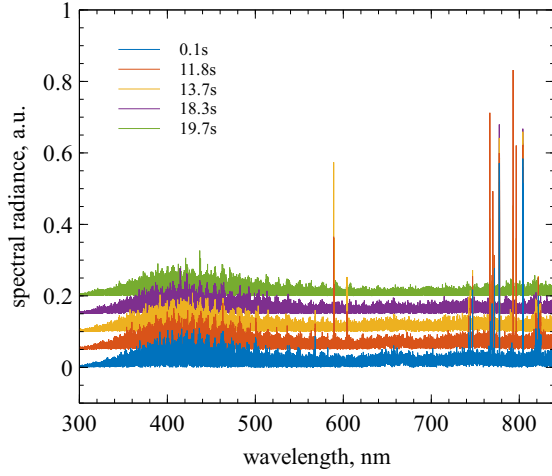
Fig. 14 Still frame of aluminum 7075 test at 75 km scenario 1

Spectral data of the tests at the 75 km condition are displayed in Fig. 15.

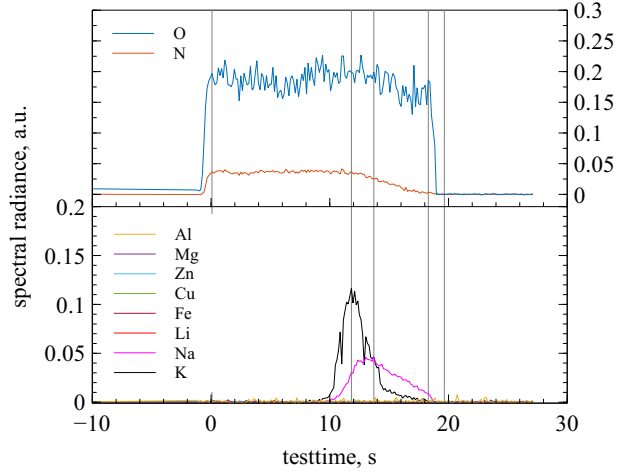
The scenario 2 experiment was conducted in the latter half of the campaign, therefore the data is less noisy than at the scenario 1 condition. One obvious oddity is the fact that the sample with an applied force during the experiment (scenario 2) survived longer than without. It is assumed that this is an error in the applied condition. This explains some of the obvious discrepancies in the temporal evolution of the species. The air plasma lines are less pronounced than in the scenario 2 test, while the alkali metals are stronger.

In the same manner as the experiments with Al-6060 aluminum none of the alloy constituents are visible spectrally. Solely the plasma lines as well as alkali metals are visible. In the tests, K appears first at around 9 s and 12 s respectively. In the scenario 1 test, K peaks at 12 s and weakens towards until it is no longer visible at 18 s, shortly before the end of the experiment at 19 s. In the scenario 2 test, K peaks at 18 s and then weakens slightly until the end of the experiment at 21 s.

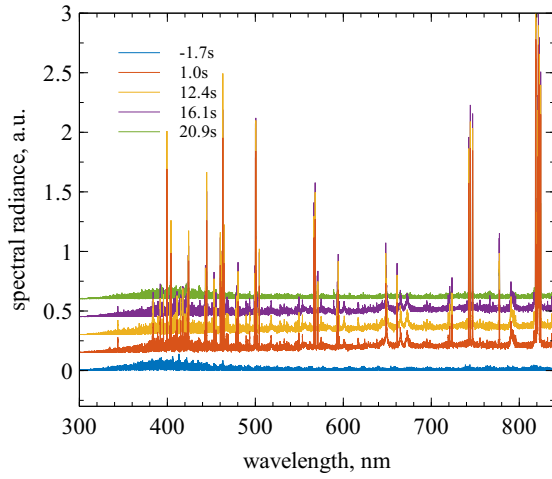
Na appears at 10 s and 14 s respectively. In the scenario 1 test the evolution is very similar to that of K, the Na line peaks at 14 s and diminishes up until the test end. The same is true for the scenario 2 test, Na peaks at 19 s and weakens slightly until the end of experiment.



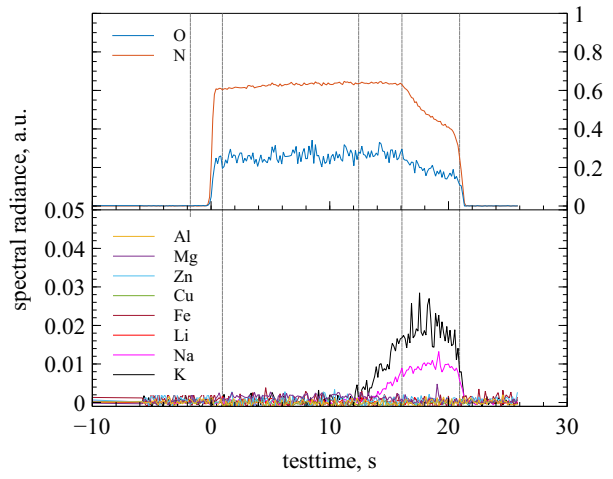
(a) Scenario 1 spectra at five test times of interest, marked in Fig. 15b



(b) Scenario 1 spectral radiance of the individual lines over time



(c) Scenario 2 spectra at five test times of interest, marked in Fig. 15d



(d) Scenario 2 spectral radiance of the individual lines over time

Fig. 15 Echelle data of Al-7075 at 75km

3. 90km

Data collected during the 90 km condition experiment is shown in Fig. 16. The experiment combined both the scenario 1 and 2 condition due to the sample not failing during scenario 2. The experiment was carried out in the first half of the campaign. The condition represents a very low pressure and low heat flux, therefore the lines are very weak. No lines aside from the plasma lines were distinguishable during testing.

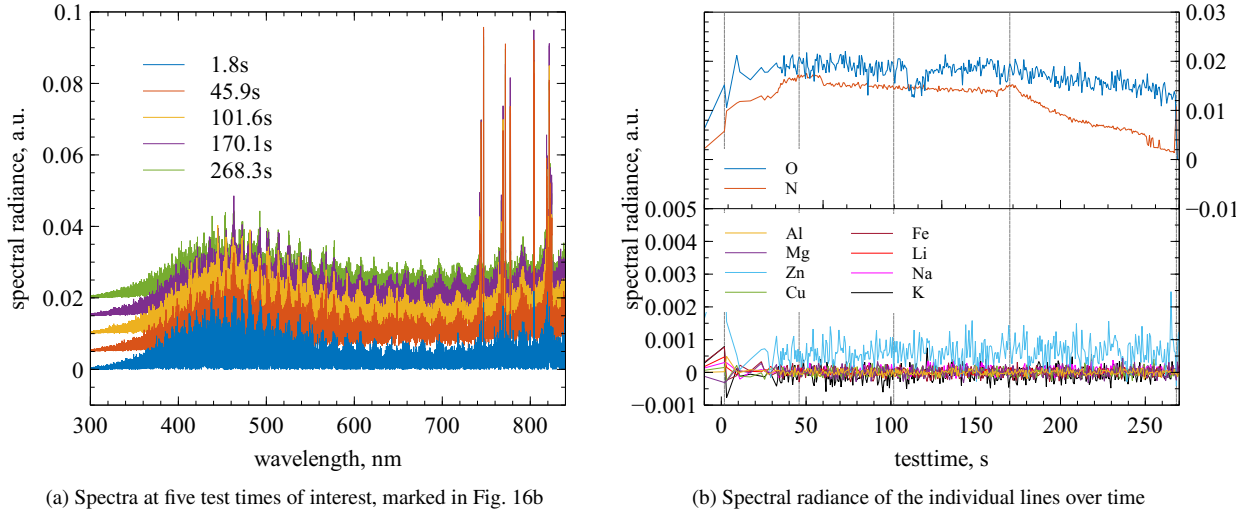


Fig. 16 Echelle data of Al-7075 at 90km scenario 1/2

IV. Analysis and Comparison to Flight

Published data on the re-entry from low earth orbit is limited, the only data known to the authors is of the observations campaigns of ATV-1 [28, 29] and Cygnus OA-6 [2, 30]. During the re-entry observation of the CYGNUS OA-6 spacecraft, sodium and lithium were detected. During the ATV re-entry observation, the presence of lithium was detected from the structural break-up explosion onward and peaked later into the entry. This was assumed to be a result of the lithium-ion (LiMnO_2) batteries [31] being damaged. However, the fact that manganese lines appeared later speaks to the contrary [20].

At the 90 km test, only spectral lines attributed to the air plasma are visible. No significant changes occur and no other lines have been identified. This behaviour fits to the re-entry simulations and observations in that no major structural material failure occurs at these altitudes.

At the 75 km condition the material failure was always preceded by the emission of alkali metals, regardless of the applied strength and the resulting variation in failure mode. A very weak potassium signature is visible in the last 5 s–10 s of all tests at 75 km. The emission of sodium at different strengths is also visible in all experiments, the emission of lithium is specific to the Al-6060 alloy and dominant in the case with no force and a melting sample.

In comparison to the observed and simulated re-entries, 75 km is equivalent to the break-up altitude of spacecraft entering from low-earth orbit. A strong onset of alkali metal emission may be used to better determine the time and thus the altitude of the main spacecraft break-up.

The 65 km condition shows similar features as the 75 km condition, all spectra show the emission of potassium shortly before failure. However the emission of sodium is particular to Al-6060 and the emission of lithium is visible

upon the material melting. As the condition that is representative of the altitude that features internal component exposure such as reaction wheels, batteries and electronic components, as well as being the trajectory point of peak heating many species are visible in the spectra of re-entry observations. It was therefore expected that more alloying elements would be visible in the experiments. The authors assume that the presence of alloying or base elements is a sign of material demise rather than structural break-up.

The new insights collected during this analysis speaks to the fact that the presence of alkali metal emission is due to the material failure of structural components made of aluminum alloys. A major difference between the test and re-entry is the fact that no alloying elements were visible in any of the test, while they are observed through large portions of re-entry observations. One possibility is that alloying elements only appear later in the demise process. Smaller components that have broken off are exposed to a higher heat flux, this expedites melting and dispersion to smaller particles. Since all experiments were ended upon the sample failure no information was obtained on the spectral response of demising aluminum alloys.

These observations show that even though the alkali metals, potassium, sodium, and lithium are not alloying elements of the aluminum alloys Al-6060 and Al-7075 they appear in direct correlation with the material failure. While potassium and sodium appear throughout the materials and conditions lithium is only visible in experiments featuring Al-6060 and most prominently upon the bulk material melting.

The authors therefore recommend to review the observed alkali metal emission in past observations and focus for these features in future re-entry observation missions. The emission of lithium from battery failure may be easily separated from the structural failure of aluminum structures and give more insight into the degradation of spacecraft aluminum structures.

V. Conclusion

Aluminum alloys were tested at conditions representative for typical flight paths. The three conditions correspond to trajectory points at early entry, break-up, and demise. The materials were tested under combined thermochemical and aeromechanical loads in a plasma wind tunnel facility with applied mechanical forces. The first interesting feature is that the analysis of emission spectra recorded with an Echelle spectrometer shows no emission of alloying elements. However strong signals corresponding to the alkali metals lithium, sodium, and potassium were detected. This is the second main result: These emissions occur shortly before the samples failed. It stands to reason that the emission of these elements can be used as an indicator of the failure of these materials during re-entry observation missions. The third finding is that a comparison of these ground tests to spectra recorded during re-entry of Cygnus OA-6 S.S. *Rick Husband* and ATV-1 *Jules Verne* show an earlier than expected emission of sodium and lithium in particular. Lithium was specifically attributed to the battery systems while sodium was thought to have originated from human waste. The new findings during this analysis might lead to a different interpretation. Future re-entry observation missions

should therefore focus on alkali metals as indicators of material failure. As the alkali metals are strong emitters, trace amounts may already be detected early on. While the bulk of the spacecraft is intact, the observation of alkali metals is most likely only from structural materials. After the main fragmentation event, additional care must be taken to separate possible sources. In the case of lithium-ion (LiMnO_2) batteries, the detection of manganese could be a direct indicator of battery failure. The fact that no alloying elements were detected in ground testing, but that strong signals were recorded during re-entry observations points to these elements being released during the demise of aluminum components. This paper concludes that fragmentation of aluminum can be detected by alkali metal line emission.

Acknowledgments

The authors gratefully acknowledge the financial support by the German Aerospace Center (DLR) through the research grant No. 50LZ1704. The dedicated support of the institute's workshop is indispensable and gratefully acknowledged. The authors would like to thank the colleagues from the High Enthalpy Flow Diagnostics Group for their continuous support.

References

- [1] ESA Space Debris Office, "ESA's Annual Space Environment Report," Tech. Rep. GEN-DB-LOG-00288-OPS-SD, ESA ESOC, May 2021.
- [2] Loehle, S., Zander, F., Lemmens, S., and Krag, H., "Airborne Observations of Re-entry Break-up: Results and Prospects," *7th European Conference on Space Debris*, ESA, Darmstadt, Germany, 2017.
- [3] Feistel, A. S., Weaver, M. A., and Ailor, W. H., "Comparison of Reentry Breakup Measurements for Three Atmospheric Reentries," *6th IAASS Conference: Safety is Not an Option*, 2013.
- [4] Loehle, S., Wernitz, R., Herdrich, G., Fertig, M., Röser, H.-P., and Ritter, H., "Airborne Re-entry Observation Experiment SLIT: UV Spectroscopy during Stardust and ATV1 Re-entry," *CEAS Space Journal*, Vol. 1, No. 1, 2010. <https://doi.org/10.1007/s12567-010-0005-3>.
- [5] Jenniskens, P., "Observations of the Stardust Sample Return Capsule Entry with a Slitless Echelle Spectrograph," *Journal of Spacecrafts and Rockets*, Vol. 47, No. 5, 2010. <https://doi.org/10.2514/1.37518>.
- [6] Loehle, S., and Jenniskens, P., "High Resolution Spectroscopy of the Hayabusa Re-entry using a Fabry-Perot Interferometer," *Journal of Spacecrafts and Rockets*, Vol. 51, No. 6, 2014, pp. 1986–1993. <https://doi.org/10.2514/1.A32480>.
- [7] Jenniskens, P., Albers, J., Koop, M., Odeh, M., Al-Noimy, K., Al-Remeithi, K., Al Hasmi, K., Dantowitz, R. F., Gasdia, F., Loehle, S., Zander, F., Hermann, T., Farnocchia, D., Chesley, S. R., Chodas, P. W., Park, R. S., Giorgini, J. D., Gray, W. J., Robertson, D. K., and Lips, T., "Airborne Observations of an Asteroid Entry for High Fidelity Modeling: Space Debris Object WT1190F," *SciTech 2016*, AIAA, 2016.

- [8] Leiser, D., Loehle, S., Zander, F., Choudhury, R., Buttsworth, D., and Fasoulas, S., "Spacecraft Material Tests under Aerothermal and Mechanical Reentry Loads," *AIAA Scitech 2019 Forum*, AIAA, 2019.
- [9] Loehle, S., Fasoulas, S., Herdrich, G., Hermann, T., Massuti-Ballester, B., Meindl, A., Pagan, A. S., and Zander, F., "The Plasma Wind Tunnels at the Institute of Space Systems: Current Status and Challenges," *46th Aerodynamic Measurement Technology and Ground Testing Conference*, AIAA, 2016. <https://doi.org/10.2514/6.2016-3201>.
- [10] Leiser, D., Loehle, S., Zander, F., Buttsworth, D., Choudhury, R., and Fasoulas, S., "Analysis of Re-entry and Break-up Forces from Impulse Facility Experiments and Numerical Rebuilding," *manuscript submitted for publication*, 2021.
- [11] Lips, T., "Private Communication of ESA report 40000110952/14/NL/PA," , 03 2020.
- [12] ESA DIVE Study team, "DIVE - Guidelines for Analysing and Testing the Demise of Man Made Space Objects During Re-entry," Tech. Rep. ESA-TECSYE-TN-018311, ESA estec, 2020.
- [13] Beck, J., Holbrough, I., and T., S., "Characerisation of Behaviour of Critical Elements in Re-Entry Conditions: Final Report," Tech. Rep. ESA: 4000126031/18/NL/GCL/as, Belstead Research Ltd., 2020.
- [14] Koppenwallner, G., Fritsche, B., Lips, T., and Klinkrad, H., "SCARAB - A Multi-Disciplinary Code for Destruction Analysis of Spacecraft during Re-entry," *5th European Symposium on Aerothermodynamics for Space Vehicles*, ESA, 2005.
- [15] Lips, T., Loehle, S., Marynowski, T., Rees, D., Stenbeak-Nielsen, H. C., Beks, M. L., and Hatton, J., "Assessment of the ATV-1 Re-Entry Observation Campaign for Future Re-Entry Missions," *IAASS Conference*, IAASS, 2010.
- [16] Loehle, S., "Review of Heat Flux Measurements for High Enthalpy Flows," *32nd AIAA Aerodynamic Measurement Technology and Ground Testing Conference*, AIAA, 2016. <https://doi.org/10.2514/6.2016-3205>.
- [17] Leiser, D., Loehle, S., and Fasoulas, S., "A Novel Approach to Flight-to-Ground Scaling in Plasma Facilities: Axisymmetric to Planar Transformation," *International Conference on Flight Vehicles, Aerothermodynamics and Re-entry Missions and Engineering*, 2019.
- [18] Stöckle, T., "Untersuchung der Oberflächenkatalyzität metallischer und keramischer Werkstoffe in Hochenthalpieströmungen," Dissertation, Universität Stuttgart, Institut für Raumfahrssysteme, 2000.
- [19] Leiser, D., Loehle, S., Hufgard, F., and Fasoulas, S., "Theoretical and Experimental Analysis of Flight-to-Ground Scaling for Axisymmetric and Planar Bodies," *AIAA Scitech 2020 Forum*, AIAA, 2020.
- [20] Lips, T., Koppenwallner, G., Rees, D., Stenbeak-Nielsen, H. C., Beks, M. L., Loehle, S., Weikert, S., and Kudo, G., "Assessment of the ATV-1 Re-entry Observation Campaign for Future Re-entry Missions," Final Report 22666/09/NL/AF, Hypersonic Technology Göttingen, 2011.
- [21] DIN EN 573-3:2019-10, "Aluminium and aluminium alloys - Chemical composition and form of wrought products - Part 3: Chemical composition and form of products," Standard, DIN e.V., Berlin, DE, Oct. 2019.

- [22] Loehle, S., Hermann, T., Zander, F., and Marynowski, T., “Echelle Spectroscopy for High Enthalpy Flow Diagnostics,” *46th Aerodynamic Measurement Technology and Ground Testing Conference*, AIAA, 2016.
- [23] Sansonetti, J. E., and Martin, W. C., “Handbook of Basic Atomic Spectroscopic Data, NIST Standard Reference Database 108,” Tech. rep., National Institute of Standards and Technology, Nov. 2013. <https://doi.org/10.18434/T4FW23>.
- [24] Liu, Y., Lin, J., Huang, G., Guo, Y., and Duan, C., “Simple empirical analytical approximation to the Voigt profile,” *Journal of the Optical Society of America B*, Vol. 18, No. 5, 2001, pp. 666–672.
- [25] Olivero, J. J., and Longbothum, R. L., “Empirical Fits to the Voigt Line Width: A Brief Review,” *Journal of Quantitative Spectroscopy and Radiative Transfer*, Vol. 17, 1977, pp. 233–236. [https://doi.org/doi:10.1016/0022-4073\(77\)90161-3](https://doi.org/doi:10.1016/0022-4073(77)90161-3).
- [26] Pearse, R. W. B., and Gaydon, A. G., *The Identification of Molecular Spectra*, 4th ed., Chapman and Hall, 1976. ISBN 0 412 14350 X.
- [27] Hermann, T., Loehle, S., Fasoulas, S., and Andrianatos, A., “Tomographic Optical Emission Spectroscopy for Plasma Wind Tunnel Testing,” *Applied Optics*, Vol. 55, No. 36, 2016, pp. 10290–10298. <https://doi.org/10.2514/6.2016-3203>.
- [28] Mazoué, F., Beck, J., and Reynier, P., “Review and Assessment of ATV Observation Data for Events Characterization,” *4th International Workshop on Radiation and High Temperature Gases in Atmospheric Entry*, Lausanne, 2010.
- [29] Marynowski, T., “Analyse und Auswertung der spektroskopischen Messdaten des Wiedereintritts von ATV1 “Jules Verne”,” Diplomarbeit, Universität Stuttgart ITLR, Jan. 2010.
- [30] Loehle, S., Eberhart, M., Zander, F., Meindl, A., Rudawska, R., Koschny, D., Zender, J., Dantowitz, R., and Jenniskens, P., “Extension of the Plasma Radiation Database PARADE for the Analysis of Meteor Spectra,” *Meteoritics and Planetary Science*, 2021. <https://doi.org/10.1111/maps.13622>.
- [31] Lagattu, B., and Granger, J.-F., “Human Flight Batteries Ni-Cd/Li-MnO₂,” *Proc. 9th European Space Power Conference*, 2011. ESA SP-690.